Solar sail propulsion limitations due to hydrogen blistering

M. Sznajder[a,*], P. Seefeldt[a,*], T. Spröwitz[a], T. Renger[a], J. H. Kang[b], R. Bryant[c], W. Wilkie[c]

[a]*German Aerospace Center (DLR), Institute of Space Systems, Mechanics and Thermal Systems, 28357 Bremen, Germany*
[b]*National Institute of Aerospace, Hampton, 23666 VA, United States of America*
[c]*NASA Langley Research Center, Hampton, 23681-2199 VA, United States of America*

Abstract

Metallized thin films are commonly considered for solar sail membranes operating in the interplanetary space. A key characteristic of this environment is the solar wind, with its charged low energy <10 keV particles. Aluminum subjected to low energy protons undergoes recombination processes between protons and metal electrons, resulting in the formation of blisters on the surface. Blistering results in degradation of the reflective properties of the solar sail membrane. Specimens were tested at environmental conditions derived from a conceptual sub-L1 mission. They were exposed to 2.5 keV protons at temperatures between −176°C and 113°C. The exposed samples exhibited visible color changes; from shiny metallic to dim light gray. Reflectivity measurements revealed reductions in specular reflectance, which results in changes to the propulsion characteristics of a sailcraft subjected to similar environmental conditions.

Keywords: Solar sailing, hydrogen blistering

Nomenclature

A	Area
a_i	reflection coefficient
a_c	characteristic acceleration
α_S	Solar absorptance
α	Pitch angle of sail
B	Non-Lambertian coefficient
c	Speed of light
F	Force
λ	Wavelength
m	Mass
R	Specular reflectance
ρ	Reflection coefficient
S	Solar constant
s	Specular reflectance factor
σ	Stefan-Boltzmann constant

*Corresponding authors, Maciej.Sznajder@dlr.de and Patric.Seefeldt@dlr.de

1. Introduction

The principle of solar sailing depends on specular reflection efficiency of its membrane material. Only with the specular reflection it is possible to change orbit energy and fly interplanetary trajectories. A decrease of reflectivity would have a significant impact on solar sail missions, especially “on the trip times and on the optimal steering profile” Dachwald et al. (2005).

The solar sail community often considers thin aluminized polymer films as lightweight membrane reflector material. Our studies show that such reflectors severely lose their specular reflectance under proton irradiation as present in the solar wind. The process responsible for this is hydrogen blistering. It is described in more detail in Section 2. Protons recombine with free electrons of the metal lattice to hydrogen and form microscopic bubbles on the surface which change the surface from a specular reflective to a more diffuse reflective one.

The aim of the work presented here is to quantify the reflectance loss over mission time in order to better understand its impact on solar sail missions. This is done by analyzing a reference mission (Section 3) with respect to its trajectory and expected sail temperatures and link this data to the expected proton flux (Section 4). Based on this analysis conditions for different proton radiation tests are defined in order to partially recreate

the space environment in the laboratory as described in Section 5.1. Specimens of a membrane material (double aluminized polyimide, Upilex-S) were then subjected to the proton radiation at different temperatures and constant proton energy as shown in Section 6. After the radiation test the loss of specular reflectance was measured with a Bruker 80v FTIR spectrometer (see Section 6.7).

The here presented results are a continuation of a series of experiments on hydrogen blistering phenomenon under simulated interplanetary space conditions. Previous work took into consideration proton fluence Sznajder et al. (2015) and magnitude of proton flux Sznajder et al. (2018) on dynamics of the blister growth. Now, influence of a target material temperature on the blistering phenomenon is studied.

2. Hydrogen blistering - principles

Hydrogen blistering is classified as one of the processes of the so-called hydrogen embrittlement (HE) class of phenomena Myers et al. (1992). HE causes irreversible changes of materials physical properties. Surface blistering is a result of hydrogen agglomeration within the metal lattice.

In space, hydrogen is created in metals by recombination processes Hagstrum (1965); Sols and Flores (1984); Eichler (2005) of solar wind protons and electrons present in the metal lattice. For this to happen, protons must have an energy low enough to stop within the thin metallic layer. If the energy is too high, protons go through it and eventually get stuck within the underlying substrate or they go through the whole material. Solar sail membrane material is continuously exposed to a flux of protons which results in an increasing concentration of a recombined hydrogen within its thin metallic layer. From the first moments of being exposed to solar wind protons, the recombined hydrogen starts to bind to metal vacancies and then it agglomerates into H_2-clusters that finally appear as small metallic pockets on the membrane surface. Average blister radius is $\sim 0.2\mu$m Sznajder et al. (2015). One can see the blister population by eye as light grey surface slowly appearing, as proton exposure progresses on the metallic surface, see Section 6. In order to give impression how aluminum surface looks like under a microscope, a double aluminized polyimide was exposed to protons with energy of 2.5 keV protons, flux of 2×10^{12} $p^+cm^{-2}s^{-1}$, fluence of 2.2×10^{17} p^+cm^{-2} and temperature of 31.6°C, see Fig. 1. Those are equal parameters to the here presented sample S3, see Section 5.3. The picture is a 2D Atomic Force Microscope (AFM) image of 5x5 μm^2 viewfield (Fig. 1(a)) and it shows sample surface covered with H_2 blisters. A 3D AFM picture of the surface with larger viewfield of 20x20 μm^2 is shown in Fig. 1(b). Here once can see that height of the blisters is dependent on their size. The largest once have height of $\sim$100 nm which is comparable to the thickness of the aluminum film.

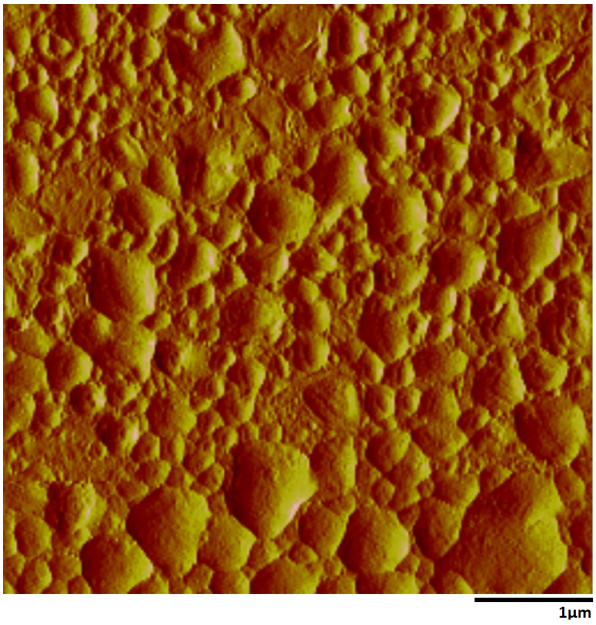

(a) A 2D 5x5 μm^2 viewfield of Al sample exposed to 2.5 keV p^+.

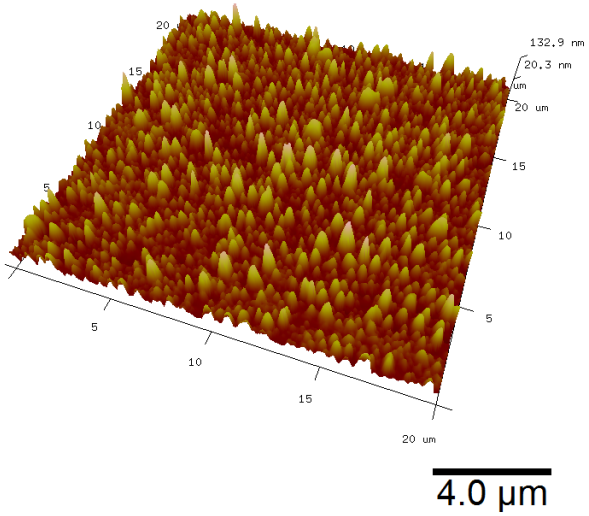

(b) A 3D 20x20 μm^2 viewfield of Al sample exposed to 2.5 keV p^+.

Figure 1: AFM pictures of a double aluminized polyimide film exposed to 2.5 keV p^+.

The phenomenon only appears under certain environmental conditions. The main parameters are: an energy,

a proton flux and a fluence magnitude as well as a specimen temperature. Their role in the blistering process is explained in the following paragraphs.

The energy of the protons must be low enough that the protons get stuck within the aluminum layer. For a 100 nm thick Al coated with ~5 nm thick native AlOx layer Evertsson et al. (2015), about 95.9% of 4 keV protons stay in the aluminum layer, 4% can be backscattered and rest (0.1%) is transmitted to the substrate. In case of 2.5 keV protons, 94.9% stuck within the aluminum layer and 5.1% can be backscattered. Hence, energy of ≤4 keV allows to study proton-Al ion interactions without influence of a substrate material. For the presented studies, 2.5 keV protons have been used in order to form the H_2-blisters. Stated here numbers have been obtained by use of the SRIM software Ziegler et al. (2010) and are standard output information out of collision simulation. Visual impression how protons penetrate aluminum is given in Fig. 2. There, two study cases are shown. On each picture, the surface of an aluminum film is located on the left side. Also, protons strike the target in one point. This is indicated by an arrow. The two cases represent a film irradiated by 2.5 keV and 4.0 keV protons on Fig. 2(a) and Fig. 2(b), respectively. Here, green and blue points represent recoils, while the red once the incident protons penetrating target material. Comparing both pictures one can see that 2.5 keV protons are implanted more in the first half thickness of the film, while for energy of 4.0 keV more protons are in the center of the film thickness. This visual impression corresponds to average penetration depths of the protons for the considered cases. It is ~30 nm for 2.5 keV protons and ~43 nm for 4.0 keV protons Ziegler et al. (2010).

The proton flux must be below $\approx 2.27 \times 10^{12}$ $p^+cm^{-2}s^{-1}$ Sznajder et al. (2018). Aluminum native AlOx layer acts as a diffusion barrier for the recombined hydrogen. However, when exposed to the mentioned proton flux, it cracks. Cracks allow hydrogen to escape from the metal lattice and the blister process is significantly decelerated. In space, average flux of solar wind protons at 1 AU is in order of $\bar{f} \sim 10^8$ $p^+cm^{-2}s^{-1}$ for proton energies ≤ 10 keV. More information about the solar wind proton flux magnitudes can be found in the Section 4.

The proton fluence must exceed 10^{16} p^+cm^{-2} Milacek and Daniels (1968). However from our studies blisters appear on the vacuum deposited aluminum surface when the fluence is $\geq 10^{17}$ p^+cm^{-2}.

The temperature significantly influences the diffusion process and thereby the appearance of blisters. For lower temperatures, we tested down to −176°C, the diffusion rate is lower and the blistering appears slower. However, the accumulated hydrogen rapidly forms blisters when the irradiated sample is heated up. At elevated temperatures, our highest temperature tested was 113°C, the diffusion rate increases, and therefore, the lattice energy prevents formation of stable H_2-clusters which consequently leads to a significant drop of surface density of the blisters.

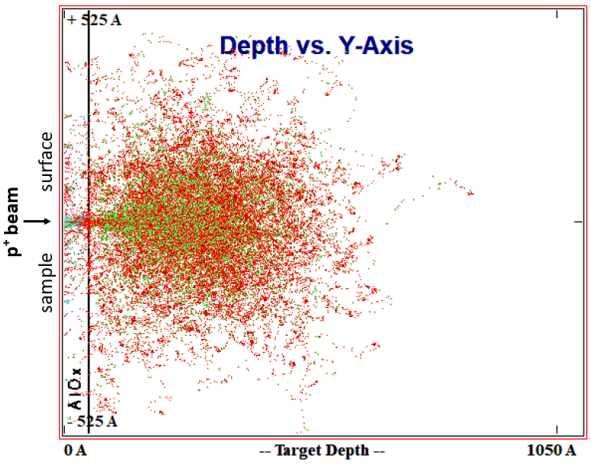

(a) Distribution of 2.5 keV p^+ penetrated within aluminum film.

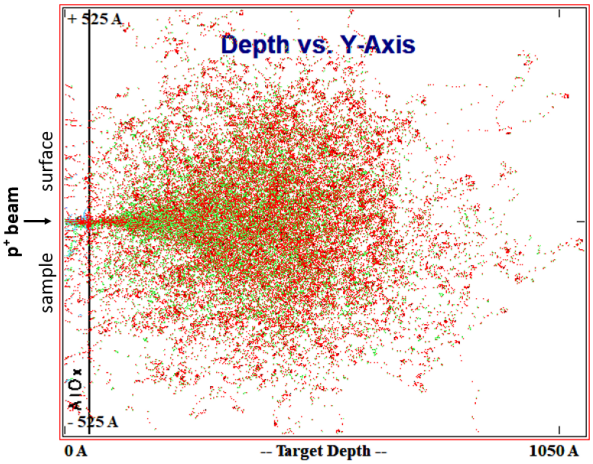

(b) Distribution of 4.0 keV p^+ implanted within aluminum film.

Figure 2: 100 nm Al film coated with 5 nm thick AlOx exposed to 1000 protons with energy of 2.5 keV (a) and 4.0 keV (b).

There are also studies which show that a high number of impurities and defects within metal structure Daniels (1971) accelerate blister formation. Also, crystallographic orientation of the target material Xie et al. (2015) influences the blistering phenomenon.

3. Reference mission

The solar sail mission architectures assumed for this study are based on small satellite solar sail systems and technologies under development at NASA Langley Research Center (NASA LaRC). These solar sail systems use new deployable composite boom technologies that are being developed by NASA LaRC and the German Aerospace Center (DLR). In 2016, NASA LaRC built and ground-tested a 9.2 m by 9.2 m composites-based engineering development unit (EDU) solar sail system suitable for a 6U CubeSat spacecraft Fernandez et al. (2018). An improved version of the composites-based EDU solar sail – the Advanced Composites-Based Solar Sail System (ACS3) - is currently in development by NASA LaRC and NASA Ames Research Center for a low Earth orbit (LEO) solar sail technology risk reduction mission with launch in the 2021 timeframe Wilkie et al. (2019). The 12U ACS3 flight experiment is intended as a technology development pathfinder for a future, larger small satellite solar sail system suitable for 12U to 27U CubeSat class spacecraft.

For purposes of this study, a trajectory for a notional near-term solar sail mission in the vicinity of 1 AU was used to estimate representative solar radiation exposure and thermal testing conditions. The notional mission was based on trajectories considered for the NASA 'Sunjammer' project Heiligers et al. (2014), although lightness numbers consistent with anticipated future ACS3 solar sail technology solar sails were assumed. While a structural analysis for the overall reflectance of the sail was taken into account, the reflective membrane itself is considered ideal reflective. Four mission scenarios were analyzed. Two mission scenarios for an artificial equilibrium point (AEP) in the sub-L1 region with a trailing angle of 5° and two scenarios for a fly-out from Earth GTO into a Halo orbit were analyzed, each for lightness numbers β of 0.02 and 0.025:

- C1a: AEP, $\beta = 0.020$
- C1b: AEP, $\beta = 0.025$
- C2a: Halo, $\beta = 0.020$
- C2b: Halo, $\beta = 0.025$

Fig. 3 shows the distance from the Sun for these four different sail trajectories.

Thermo-optical properties for several candidate solar sail membrane materials were used Kang et al. (2019) and are listed in Table 1. With sail attitude and heliocentric distance the surface incidence angle α and thermal equilibrium state of the sail membrane throughout the mission is calculated as

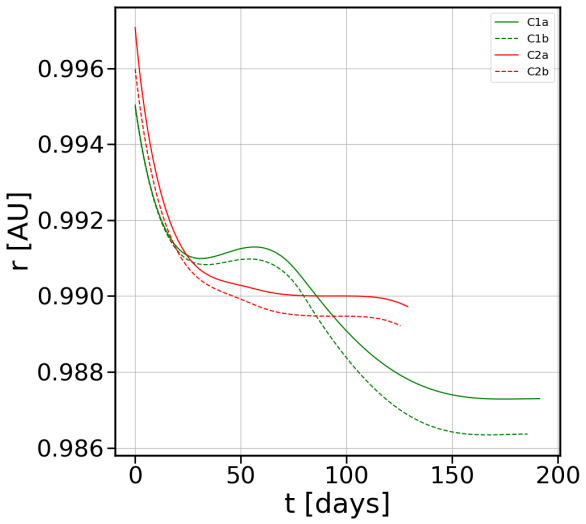

Figure 3: Distance from the Sun for different trajectories of four Lagrange point L1 solar sail mission scenarios.

$$T = \left(\frac{S \left(\frac{r_e}{r}\right)^2 \alpha_S \cos\alpha}{(\epsilon_f + \epsilon_b)\sigma} \right)^{1/4} . \quad (1)$$

Here S is the solar constant (1367 Wm^{-2}), r is the distance from the Sun, r_e is the average distance of the Earth from the Sun (1AU), and σ is the Stefan-Boltzmann constant 5.67×10^{-8} $\mathrm{Wm}^{-2}\mathrm{K}^{-4}$.

Temperature evaluated by Eq. 1 does not take into account fact that thermo-optical properties depend on material temperature Ancona and Kezerashvili (2017). However, for the here considered temperatures of the specimens, i.e. from −176°C (97K) to 113°C (386K), correction factor that $\epsilon = \epsilon(T)$ is lower than 2%. Hence, here it is considered that thermo-optical properties have *constant* values. Furthermore, during the considered reference mission to the L1 the distance to the sun is only slightly changed. For this particular mission a more precise model for the temperature dependence on the distance to the sun has no significant impact. However, the presented test results and temperatures can of course be correlated to different missions, for which more accurate modeling of the temperature can be used.

The considered membranes are coated polymer foils. While the front side is always coated with aluminum in order to provide the reflective properties, the back side is either the substrate material or another coating in order to influence the radiative properties and thereby the membrane temperature.

Table 1: Solar sail membrane material and its thermo-optical properties, solar absorptance α_S and infrared emittance ϵ for the front side (subscript f) and for the backside (subscript b).

Material	α_S	ϵ_f	ϵ_b
Al-Kapton-Cr	0.1	0.05	0.55
Al-CP1	0.1	0.03	0.31
Al-PEN-Cr	0.09	0.04	0.66
Al-PET	0.12	0.02	0.25

Fig. 4 shows temperature profiles for the different materials under consideration of the four considered trajectory scenarios.

The temperatures reached by the solar sail are relatively low. This is because the coatings of the membrane were chosen such that they have good radiative properties in order to keep it on a low temperature. In the presented studies, elevated temperatures decrease the blistering effect. As highest temperature for the test we derived, in addition to the studied missions cases, the equilibrium temperature of a membrane coated with aluminum on both sides at 1 AU distance from the Sun. The optimal α angle for a logarithmic spiral trajectory of 35.26° is used. The thermo-optical properties were measured, α_S is 0.093 and ϵ is 0.04. The equilibrium temperature is calculated as

$$T_{\max} = \left(\frac{S\,\alpha_S \cos\alpha}{2\epsilon\sigma}\right)^{1/4} = 112.77^\circ \text{ C}. \tag{2}$$

4. Interplanetary space environment and the mission proton fluence

Interplanetary space environment is determined strongly by the Sun activity. Its ~11-year cycle results in modulations of electromagnetic radiation irradiance and amount of charged particles blown into space. Basic proton parameters like number density, speed and direction are recorded by many space Sun observatories, e.g. SOHO, ACE, WIND, or DSCOVR. Data processing of those parameters allow to estimate proton flux for each energy recorded by satellites.

Correlation between the Sun activity and the average proton flux can be analyzed from data given in Fig. 5. Fig. 5(a) gives the number of sunspots as a function of calendar year and number of solar cycle. Such data can be found e.g. in the SILSO data center SILSO World Data Center (1996-2019). Fig. 5(b) shows the average proton flux for 4 mentioned Sun observatories. Clearly, for both Sun maximum activities, i.e. year ~2001 and year ~2014, the proton flux reaches its maximum value, while at Sun minimum activity (year ~2009), the proton flux has its minimum value. Such long term modulation of the solar wind proton flux magnitude must be taken into account when considering a sailcraft mission for a time comparable to a Sun cycle period.

In order to calculate the total number of protons per square centimeter radiated on the sail membrane material, the so-called proton fluence, one must first calculate the *cumulative proton flux*. It is a sum of all of the individual proton fluxes for an energy range of interest. If one takes data from e.g. ACE Sun observatory and sum up all of the fluxes from lowest recorded energy up to the highest one (approx. 6 keV), then the cumulative flux at L1 point f_{L1} is 1.17×10^{12} $p^+cm^{-2}s^{-1}$. The here presented proton irradiation tests were made with 2.5 keV protons, therefore, for energies ≤2.5 keV the corresponding f_{L1} flux is 0.88×10^{12} $p^+cm^{-2}s^{-1}$.

The flux f_{L1} must be corrected by the pitch angle α (angle of incidence of the SW protons) and distance of the sail to the Sun $r(t)$:

$$f(t) = f_{L1}\frac{r_{L1}^2}{r^2(t)}\cos(\alpha) \tag{3}$$

Fig. 6 shows proton fluxes calculated for the four mission scenarios and the $f_{L1} = 0.88 \times 10^{12}$ $p^+cm^{-2}s^{-1}$. The flux, while the sail is changing its pitch angle, varies from almost 0-value to its maximum value of f_{L1}. Such a modulation changes the speed of blister formation. However, the driving parameter for its formation is the fluence.

Knowing the time evolution of the flux $f(t)$, the proton fluence can be calculated. Fig. 7 shows the so-called *step-fluence*. Each point of the curve is an integral solution of the flux and a time period counted from beginning to each moment of the mission period

$$F(t) = \int_0^t f(t')\,dt'. \tag{4}$$

Fig. 7(a) shows the step-fluence as a function of mission time based on the f_{L1} of 1.17×10^{12} $p^+cm^{-2}s^{-1}$, while Fig.7(b) on the f_{L1} of 0.88×10^{12} $p^+cm^{-2}s^{-1}$. The here presented proton irradiation tests were performed with fluence of 2.2×10^{17} p^+cm^{-2}, hence, for the first case, that fluence is reached after approx. 2.7 days in space, while for the second case after approx. 3.5 days in space at ~1 AU.

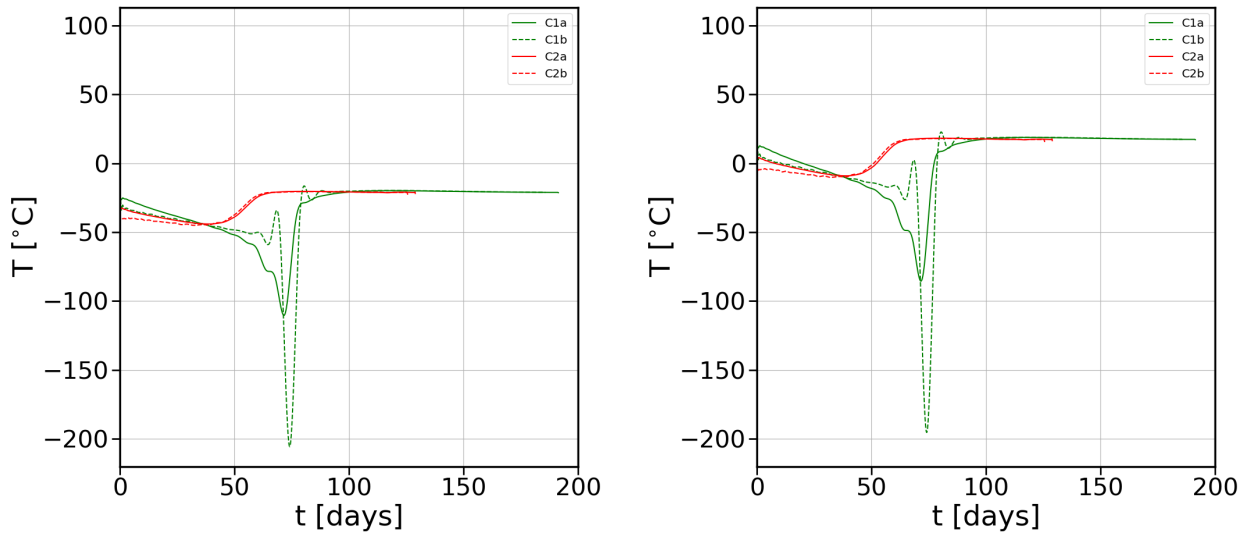

(a) Al-Kapton-Cr

(b) Al-CP1

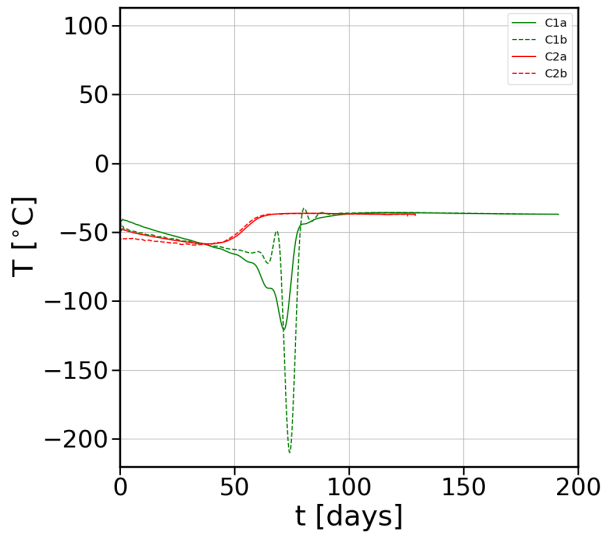

(c) Al-PEN-Cr

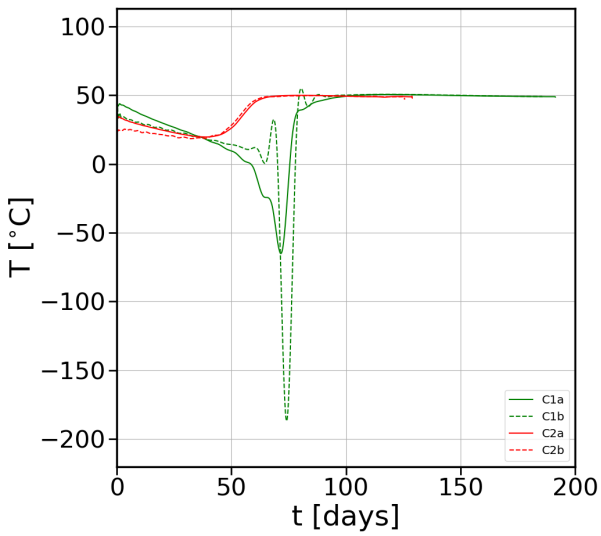

(d) Al-PET

Figure 4: Calculated temperature of the membrane throughout the mission for different scenarios and materials.

5. Test setup

To correctly simulate hydrogen blistering as it would take place in space one needs a flux of protons which then mimics Sun's stream of outflowing protons from its corona. Such approach has twofold benefits. First, in modern test facilities a beam of protons can be well defined, i.e. proton current, energy and irradiation time can be well adjusted. Second, a proton beam can be easily positioned on any location of a test sample. Irradiation must be performed under vacuum with simultaneous control of a sample temperature. Only such conditions guarantee that irradiation test results will represent those taking place under real space conditions. Radiation with protons was then carried out in DLR's Complex Irradiation Facility.

5.1. Test facility - the Complex Irradiation Facility

The Complex Irradiation Facility at DLR in Bremen can simulate solar wind consisting of electrons, protons and a wide range of electromagnetic radiation, i.e. from 40 nm to 2150 nm under ultra-high vacuum conditions

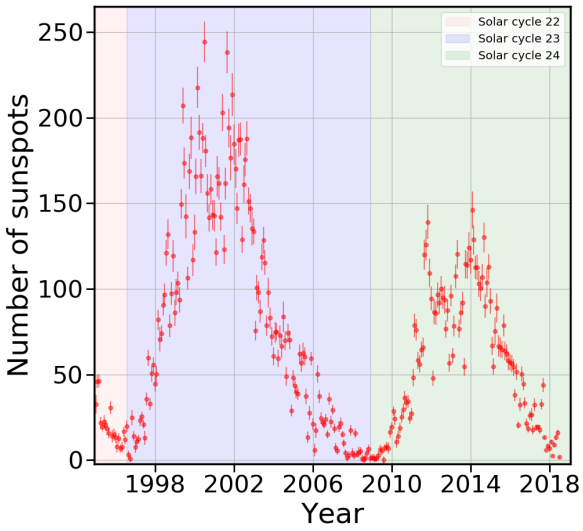

(a) Number of sunspots as a function of calendar year

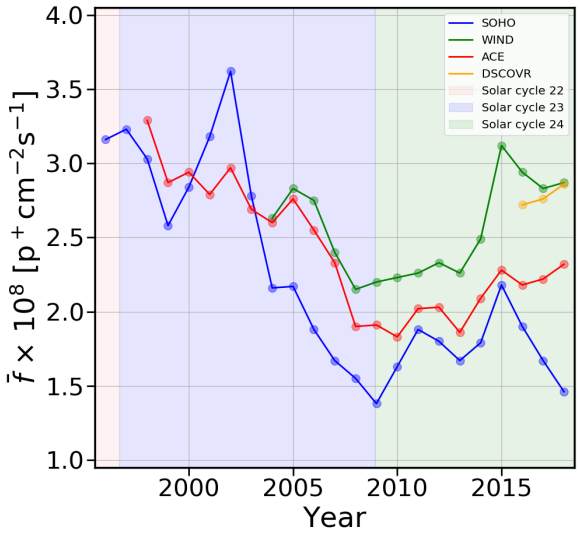

(b) Average proton flux as a function of calendar year

Figure 5: 5(a) Number of Sun spots as a function of calendar year. 5(b) Average solar wind proton flux given for each calendar year.

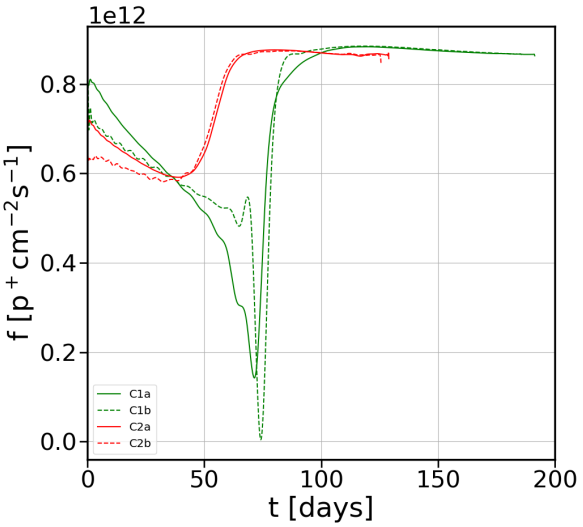

Figure 6: Proton flux evolution for four mission scenarios and based on the $f_{L1} = 0.88 \times 10^{12}$ p$^+$cm^{-2}s^{-1}.

Renger et al. (2014). Electrons and protons are generated by two linear accelerators with maximum energy of 100 keV each. Particle current can be set from 1 nA up to 100 μA. However, in the energy range from 2 keV to 10 keV maximum current is $\approx$5 μA with a spot diameter of 37 mm. Maximum exposed area is 60×60 mm^2 achieved with a beam sweep mechanism. Such conditions allow to simulate solar wind electron and proton fluxes with acceleration factor higher than 1. The facility allows to set up electron and proton beams separately, i.e. both species can irradiate target material simultaneously while having different energy and flux. Also, particle exposure can be accompanied with simultaneous illumination of test material with electromagnetic radiation. Figure 8 shows the facility and its main components.

For temperature control of the test specimens a sample station that holds the sample holder with the test object can be heated from behind by halogen lamps or it can be cooled down by LN_2.

5.2. *Temperature calibration for test specimens*

Before the irradiation test campaign was started, temperature measurements of the test material for calibration purposes were made. The foil samples were mounted on a Cu-plate using 3M transfer tape 966. For the calibration test a PT100 sensor (T1) was placed in-between the foil and the Cu-plate. The plate was then mounted with screws onto a facility specific sample holder that can be inserted into the test chamber. The setup for the temperature calibration measurement is shown in the Fig. 9.

In the cold case the lowest temperature recorded by sensor T1 was -176±1°C. Sensor T2 was 1°C colder. In the hot case, T1 = 113±1°C, sensor T2 was 1°C warmer than T1. Such an approach allows to indirectly measure the sample temperature during the irradiation test by use of just sensor T2, i.e. knowing its relation to sensor T1. Also, during irradiation test, a sample can be directly

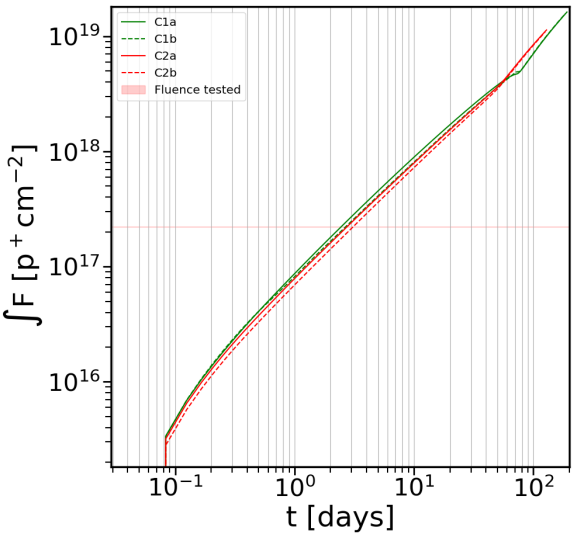

(a) Based of proton flux of 1.17×10^{12} $p^+cm^{-2}s^{-1}$

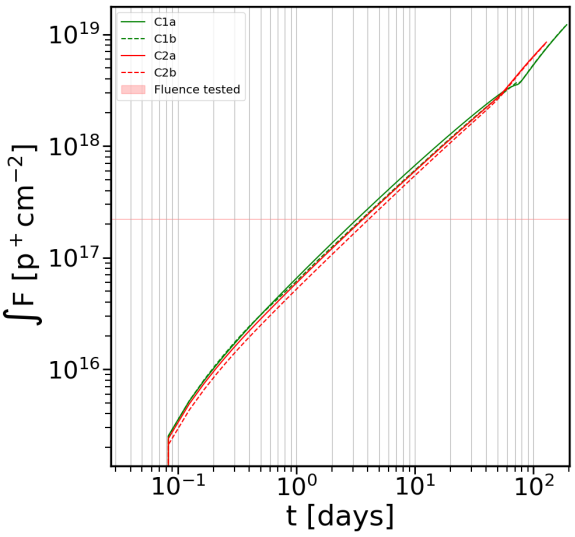

(b) Based of proton flux of 0.88×10^{12} $p^+cm^{-2}s^{-1}$

Figure 7: Step-fluence based on to different proton fluxes and calculated for four different mission scenarios.

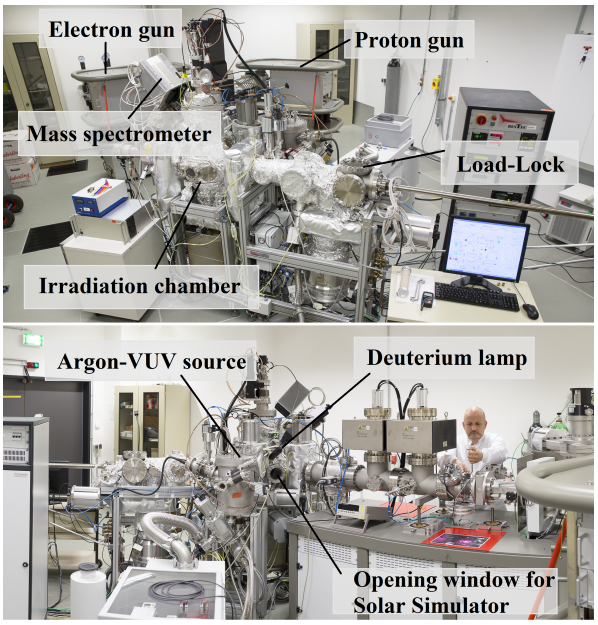

Figure 8: The Complex Irradiation Facility at DLR-Bremen.

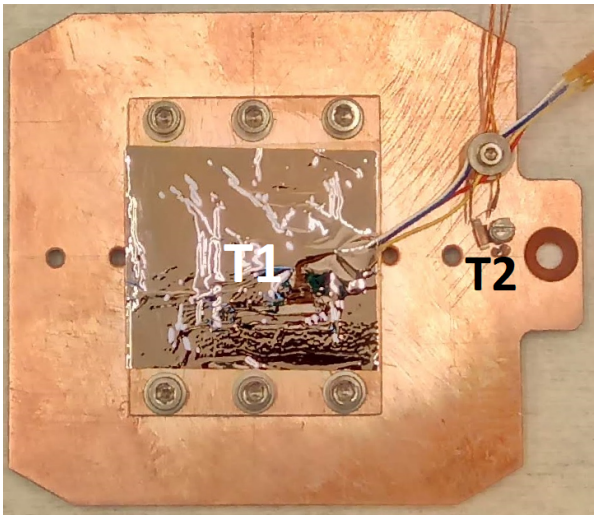

Figure 9: Two PT100 sensors mounted on the Cu-plate sample holder.

mounted on the copper plate without a temperature sensor which causes surface irregularities.

5.3. Test specimens

The material tested is from the Company UBE. It is a 7.5 μm thick Upilex-S foil that is coated with 100 nm aluminum on both sides. It seems to be reasonable that it does not matter on which substrate the aluminum coating is applied. It is believed that the results shown here are of general nature, valid for aluminum and aluminized materials. Five test samples were exposed to a well defined proton beam of 37 mm diameter at the sample position. All samples received the proton fluence of 2.2×10^{17} p^+cm^{-2} and the flux of $\approx 2 \times 10^{12}$ $p^+cm^{-2}s^{-1}$ across the spot area. The beam was orientated perpendicular to the sample surface. During tests the vacuum level oscillates around 10^{-8} mbar. The irradiation temperatures for samples S1 to S5 were −176.0°C, −100°C,

31.6°C, 75.0°C and 113°C, see Table 3.

6. Results of the proton irradiation tests

As expected the process is strongly temperature dependent and in consequence the degree of blister formation varies. The decrease of reflectance was measured with a FTIR spectrometer in order to quantify this effect for solar sail missions.

Unfortunately, during applying the foil to the Cu-plate, air was trapped in a few places between the sample foil and the Cu plate, see the sample surface S1 and S2 (Figs. 10, 11, and 12). Under ultra-high vacuum conditions this trapped air formed gas pockets which are clearly visible on the specimen surface. This effect has neither an impact on the test itself nor on the formation of H_2-blisters. The bubbles disappear when the specimen is taken out of the irradiation chamber under ambient conditions. Hence, they have no impact on the further thermo-optical properties measurements made by Bruker 80v spectrometer and hand-held reflectometer.

6.1. Sample S1

This sample has been exposed to protons at −176.0°C. However, during the test, the LN_2 bottle needed to be exchange and hence, the temperature increased to −163.2°C and a second time to −158°C. The temperature rise and decrease back to −176°C which took approx. 4h in both cases. Fig. 10 shows the sample placed inside the irradiation chamber seen through an optical window from an angle of 30°. It depicts its state before the irradiation test.

Figure 10: Sample S1 before irradiation test

Fig. 11 shows sample S1 in a few specific states during the test period. Fig. 11(a) shows the sample at 1.5 hours before the planned end of irradiation time at temperature of −174.6°C. One can see an intense spot of 37 mm in diameter. While the LN_2 flow was stopped, and the sample temperature rose to 13.3°C the visual intensity of the spot increased, Fig. 11(b). The sample was then heated up from behind by use of the halogen lamps to a temperature of 75°C, see Fig. 11(c). One can see that the intensity of the spot increased further. Then, the heating was switched off and sample reached a temperature of 16°C, Fig. 11(d). During the period when the sample cooled down again, no visual change of the spot intensity could be identified.

(a) 1.5h before irradiation ends, T=−174.6°C

(b) after irradiation phase, T=13.3°C

(c) after irradiation phase, T=75°C

(d) after irradiation phase, T=16°C

Figure 11: Sample S1 at four different stages of the irradiation test.

6.2. Sample S2

The second sample has been exposed to the protons at -100 ± 1°C. However, the temperature oscillates during the test between -98°C and -103°C. Fig. 12(a)

shows the sample surface state before start of irradiation. Fig. 12(b) depicts the sample surface at the end of the irradiation test when the specimen was still kept at -100 ± 1°C. Clearly, blisters populate the exposed surface and a light gray spot can be spotted in the center of the specimen. Then, the LN_2 cooling was switched off and the sample temperature rose to 22.3°C, see Fig. 12(c). The spot became more intense, and a light-shiny ring appeared around the spot. Next, the sample was tempered at 39.3°C for over three hours. The spot did not visually change its color, see Fig. 12(d). However, the ring became more intense and spread its dimension outwards of the spot.

Similar to sample S1, sample S2 had also air traps present on its surface while operating under UHV conditions. The bubbles disappear after sample was removed from vacuum chamber. Hence, they had no influence on further measurements of the thermo-optical properties.

6.3. Sample S3

This sample was tested in a previous study. For that reason the sample holder is slightly different, see Fig. 13. It is a metallic frame, where the material is clamped between two parts. The sample was tempered to 31.6 ± 1°C. An intense spot appeared on the specimen surface. Visually it is less intense than the samples irradiated at cryogenic temperatures.

6.4. Sample S4

In this case the sample was exposed to the protons at 75 ± 1°C. Fig. 14(a) shows the sample at room temperature, while Fig. 14(b) shows it at 75°C. There is no visual difference on the sample surface between the two temperatures. After irradiation, a slight spot can be spotted in the center of the specimen, see Fig. 14(c). Also, the spot did not change its visual properties while the heating was turned off and the sample was cooled down to 17.1°C, see Fig.14(d). Apparently, there is a significant intensity drop of the spot when a sample is exposed at 75 ± 1°C.

6.5. Sample S5

The last examined temperature within the test campaign was 113 ± 1°C. Fig. 15(a) and Fig. 15(b) show the sample surface state at room temperature and at 113.3°C, respectively. There is no visual difference between both. At the end of the irradiation time, see Fig. 15(c), a slight light gray spot appeared on the surface. The intensity of the spot remained unchanged after the specimen was cooled down to temperature of 16.6°C, see Fig. 15(d).

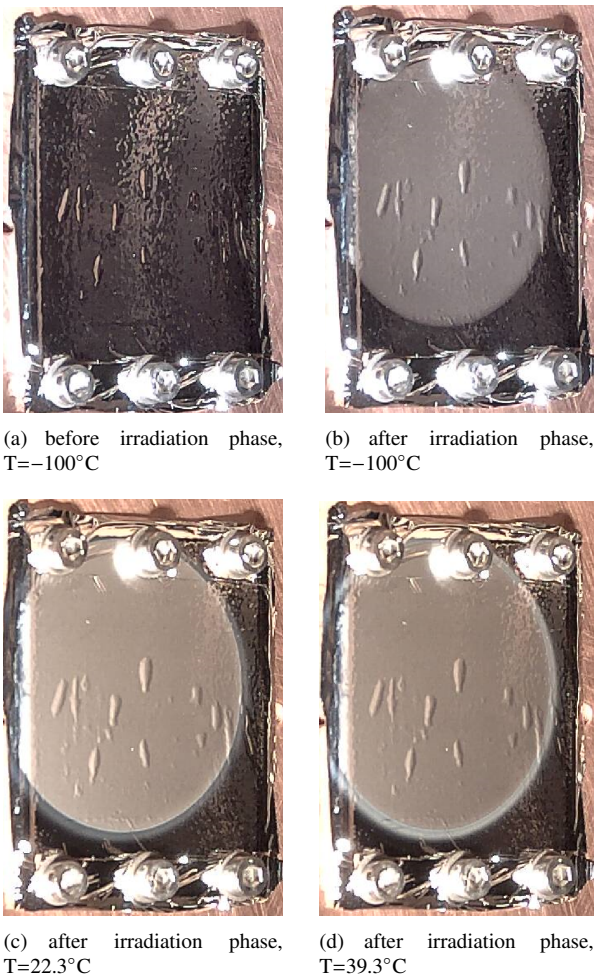

(a) before irradiation phase, T=−100°C

(b) after irradiation phase, T=−100°C

(c) after irradiation phase, T=22.3°C

(d) after irradiation phase, T=39.3°C

Figure 12: Sample S2 at four different stages of the irradiation test.

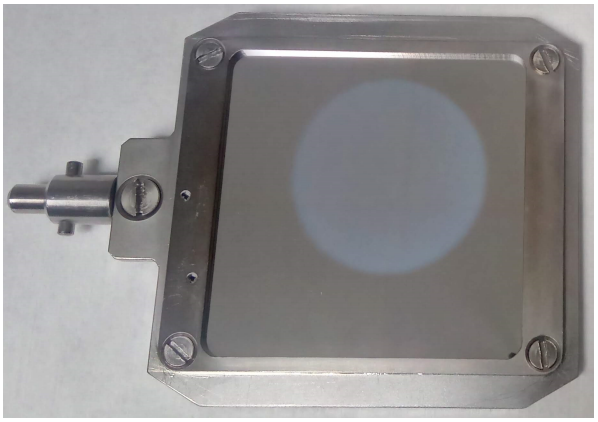

Figure 13: Sample S3

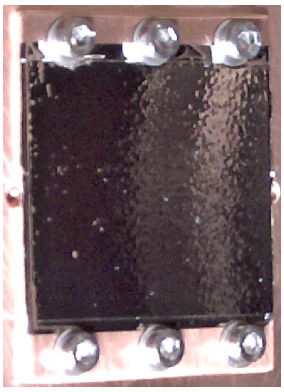

(a) before irradiation phase, room temperature

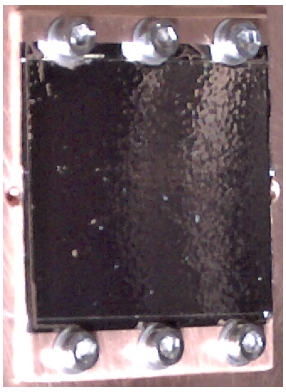

(b) before irradiation phase, T=75°C

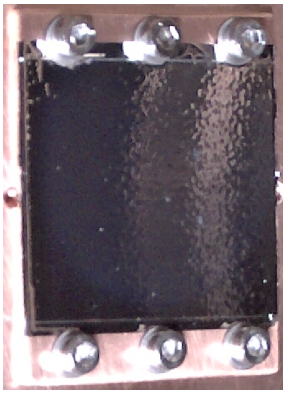

(c) after irradiation phase, T=75°C

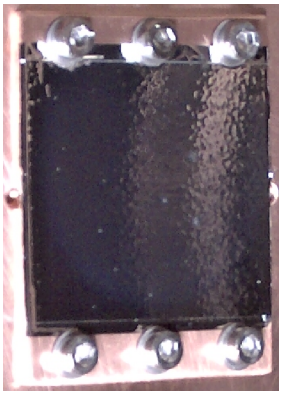

(d) after irradiation phase, T=17.1°C

Figure 14: Sample S4 at four different stages of the irradiation test.

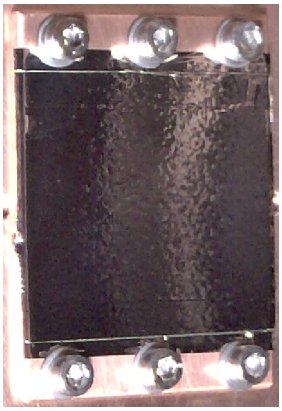

(a) before irradiation phase, room temperature

(b) before irradiation phase, T=113.3°C

(c) after irradiation phase, T=113.3°C

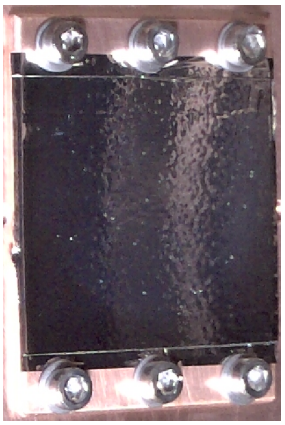

(d) after irradiation phase, T=16.6°C

Figure 15: Sample S5 at four different stages of the irradiation test.

6.6. Ring formation around spots of samples S1 and S2

The light-shiny ring observed around spots on the sample surface S1 and S2 has speculative formation explanation. Clearly, it appears only on the sample surface S1 and S2 where foil material was exposed to protons at cryogenic thermal conditions. In such conditions recombined hydrogen stuck within point defects in aluminum and its ability to move around these sites is highly limited. After irradiation is stopped and heating phase is initiated a ring starts to appear. Clearly, diffusion process in its formation was involved. Hydrogen, when a sample temperature increases, diffuses out of the spot area and starts to form a ring. Such scenario fits perfectly to the sample S2. However, for the sample S1, one can observe that just around the spot there is first a dark and then a light gray ring. The dark ring surface looks as a non-exposed material. Hence, it cannot be simply explained by diffusion of a hydrogen coming out from the exposed area, since it would have, like the sample S2, graduate discoloration from light gray to shiny metallic outwards. It must be, however, emphasized that a ring appears around an area hit by the proton beam while in space the whole sail is fully exposed to the solar wind protons so such ring-like structures won't, with high probability, appear on their membrane surface.

6.7. Specular reflectance measurements

Specular reflectance measurements were performed by use of a Bruker 80v FTIR spectrometer with a hardware configuration given in Table 2. There, the first column gives name of measured wavelength range, the second its range given in nm, the third the type of a beam splitter (BS) used in the spectrometer optics, the fourth the name of used light detector and the fifth the type of a light source (LS). For all of the measurements a halogen lamp (HL) was used as standard light source.

Table 2: Bruker 80v setup for UV-VIS-NIR measurements.

Range	λ range [nm]	BS	Detector	LS
UV	250 — 555	CaF_2	GaP	HL
VIS	455 — 1250	CaF_2	Si	HL
NIR	910 — 2500	CaF_2	DLaTGS	HL

The measurements were made with overlapping wavelength ranges. Such a procedure is applied since different light sources and detectors were used. Signals are then merged together into one curve representing reflectance of sample under study. The reflectance was measured at 35° incident angle as this is a common solar sail case for a spiral trajectory. The spectrometer was neither absolutely calibrated nor was a standard available for which the spectral data is available (this is normally used for hemispherical reflectance measurements as basis for the calculation of the solar absorptance). For this reason only comparative measurements were made. The signal strength of the exposed samples was compared to the corresponding signal of a non-degraded reference sample. The reflectance change in percent (compared to the reference sample) was calculated with the measured reflectance signal of the sample $R_S(\lambda)$ and the measured reflectance signal of the reference un-exposed sample $R_{ref}(\lambda)$

$$r(\lambda) = \frac{R_S(\lambda)}{R_{ref}(\lambda)}. \tag{5}$$

The signals were corrected for the background noise signal. The reflectance change is shown in Fig. 16. Clearly, the lower the sample temperature the larger the reflectivity drop over the whole wavelength range.

At cryogenic temperatures the hydrogen is kept in the aluminum vacancies. When cooling is stopped and temperature increases a large amount of hydrogen is released from the vacancy traps and forms H_2-clusters and then the blisters. At room and higher temperatures the recombined hydrogen can more freely migrate within the metal lattice and eventually escape from the defects through the aluminum oxide layer or diffuses into the substrate material.

The wavelength range considers 96% of the solar spectrum total energy. A good measure for the overall reflectance of the solar sail is the average specular absorption weighted with the solar reference spectrum ASTM E490 $S(\lambda)$ as

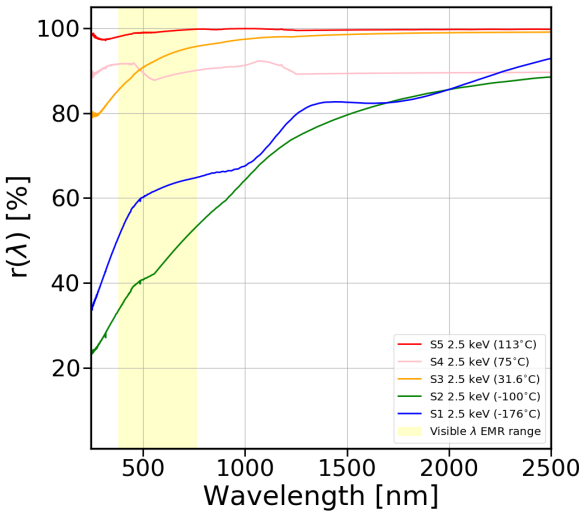

Figure 16: Relative specular reflectance as a function of wavelength range.

$$R_S = \frac{\int_{250\,\mathrm{nm}}^{2500\,\mathrm{nm}} R_S(\lambda) S(\lambda)\, d\lambda}{\int_{250\,\mathrm{nm}}^{2500\,\mathrm{nm}} S(\lambda)\, d\lambda}. \tag{6}$$

In our case we used the reflectance signal of the spectrometer for $R_S(\lambda)$ and $R_{ref}(\lambda)$ in order to measure the relative change between two samples as

$$\frac{R_S}{R_{ref}} = \frac{\int_{250\,\mathrm{nm}}^{2500\,\mathrm{nm}} R_S(\lambda) S(\lambda)\, d\lambda}{\int_{250\,\mathrm{nm}}^{2500\,\mathrm{nm}} R_{ref}(\lambda) S(\lambda)\, d\lambda}. \tag{7}$$

The calculated values for this weighted relative change of reflectance are given in Table 3. The highest reflectance drop is recorded for the sample S2. Only 66.94% of the initial reflectance is left. The smallest drop of less than 1% has sample S5.

7. Impact on the solar sail performance

It appears that the change of the surface properties is mainly caused by a change from specular to diffuse reflectance rather than a decrease of the overall reflectivity. Measurements of total reflectance ρ_{AL} and thermal emittance were performed by use of a Surface Optics hand-held reflectometer. Solar absorptance was calculated by $\alpha_S = 1 - \rho_{AL}$. The reflectance was measured from 330 nm to 2500 nm while the emittance was measured from 1500 nm to 21000 nm. All of the measurements have an accuracy of ±0.001. Results of that

Table 3: Change of relative specular reflectance weighted with the ASTM E490 reference spectrum of irradiated samples given in %-value. As reference sample the unexposed material was used. In addition the temperature during radiation and the max. curing temperature after radiation is given.

Sample	Rad. Temp. [°C]	Max. Temp. [°C]	R_S/R_{ref} [%]
S1	-176	75	73.05
S2	-100	39.3	66.94
S3	31.6	31.6	96.93
S4	75	75	90.48
S5	113	113	99.77

measurements are presented in Table 4. Pristine material as well as exposed samples from S2-S5 indicate almost the same $\rho_{AL} \sim 0.9$. Exception here is sample S1 with a total reflectance of ~0.7. That may be explained e.g. by other surface defects present in aluminum layer which were produced while rapid blister formation was taking place during heating the sample from −176°C to 75°C. Parts of the light may travel through such defects to the underlying Upilex-S substrate. Also the thermal emittance of the samples S1-S2 is two times larger than pristine material and samples S3-S5. This also may be linked to the fact that samples S1-S2 were annealed after proton irradiation phase.

Table 4: Total reflectance as well as solar absorptance and thermal emittance values of the investigated specimens.

Sample	Rad. Temp. [°C]	ρ_{AL}	α_S	ϵ
Pristine	—	0.923	0.077	0.014
S1	-176	0.693	0.307	0.025
S2	-100	0.875	0.125	0.039
S3	31.6	0.895	0.105	0.016
S4	75	0.916	0.084	0.014
S5	113	0.917	0.083	0.014

When investigating the impact on the solar sail performance it is important to not use a simple model that only considers the overall hemispherical reflectance ρ as this would suggest that a_c only undergoes a small change. Instead a model that differentiates between specular reflectance ρ_s and diffuse reflectance ρ_d must be used. The fraction $s = \rho_s/\rho = \rho_s/(\rho_s + \rho_d)$ is the specular reflectance factor. Such models are described by Dachwald et al. (2005). In this work three reflection coefficients are established:

$$a_1 = \frac{1}{2}(1 + s\rho)\,, \tag{8}$$

and

$$a_2 = \frac{1}{2}\left[B_f(1-s)\rho + (1-\rho)\frac{\epsilon_f B_f - \epsilon_b B_b}{\epsilon_f + \epsilon_b}\right] \approx \frac{1}{2}\left[B_f(1-s)\rho\right]\,, \tag{9}$$

and

$$a_3 = \frac{1}{2}(1 - s\rho)\,. \tag{10}$$

For the sake of simplicity the impact of the infrared emittance in a_2 is neglected. With these coefficients the solar radiation pressure force and acceleration can be calculated. For a first analysis of the impact of the reflection change the characteristic acceleration as well as the orbit tangential force for a sail pitch angle of $\alpha = 30°$ and orbit radius 1 AU is analyzed. Following Dachwald et al. (2005), the characteristic acceleration is calculated as

$$a_c = \frac{2SA}{cm}(a_1 + a_2), \tag{11}$$

and the tangential force for a simple 2-D case is calculated as

$$F_t = 2\left(\frac{S}{c}\right)A\cos\alpha\sin\alpha\,(a_1\cos\alpha + a_2 - a_3\cos\alpha). \tag{12}$$

Here A is the sail area, m is the sailcraft mass and c is the speed of light.

From former studies, further information about the reflectivity of pristine or degraded aluminized foil are known. This will be used to estimate the fractions of specular and diffuse reflectance of aluminized foils. (Melnik et al., 2014) presented light pressure measurements indicating that the measured force corresponds to a reflectivity (that is determined through the measured force) ρ_{LP} of about 91%. Because in this work the light pressure was measured, this can be understood in the sense that

$$
\begin{aligned}
&2 \cdot (a_{1_{\mathrm{AL}}} + a_{2_{\mathrm{Al}}}) = 1 + \rho_{\mathrm{LP}} \\
\Leftrightarrow &(1 + s_{\mathrm{AL}}\rho_{\mathrm{AL}}) + B_f(1 - s_{\mathrm{AL}})\rho_{\mathrm{AL}} = 1 + \rho_{\mathrm{LP}} \\
\Rightarrow &s_{\mathrm{AL}} = \frac{\rho_{\mathrm{LP}} - B_f\rho_{\mathrm{AL}}}{\rho_{\mathrm{AL}} \cdot (1 - B_f)}.
\end{aligned} \tag{13}
$$

Furthermore, from hemispherical reflectance measurements (for alpha determination) it is also known that the total reflectivity is about

$$
\rho_{\mathrm{AL}} = 1 - \alpha_{\mathrm{AL}} = 0.9 \ldots 0.93. \tag{14}
$$

For the sake of completeness, it should be mentioned that in Dachwald et al. (2005) the specular reflection factor is considered to be 0.94.

Knowing that for a first approximation $s = 1$ for the aluminized foil before it is subjected to proton radiation and that the overall reflectance ρ does not change by the blistering effect an estimation of the change of a_c is possible. In this case the change of the specular reflection factor and the measured change of specular reflectance $R_{\mathrm{S}}/R_{\mathrm{ref}}$ is the same

$$
s = \frac{R_{\mathrm{S}}}{R_{\mathrm{ref}}}, \tag{15}
$$

and consequently the reflectance coefficients are

$$
a_1 = \frac{1}{2}\left(1 + \frac{R_{\mathrm{S}}}{R_{\mathrm{ref}}}\rho_{\mathrm{Al}}\right), \tag{16}
$$

and

$$
a_2 \approx \frac{1}{2}\left[B_f\left(1 - \frac{R_{\mathrm{S}}}{R_{\mathrm{ref}}}\right)\rho_{\mathrm{Al}}\right]. \tag{17}
$$

According to Dachwald et al. (2005) the non-Lambertian coefficient B_f can be estimated with 0.79. It is assumed that this factor does not change for the samples subjected to proton radiation. With this a_c and F_t are described as a function of the measured specular reflectance change.

Before proton radiation the characteristic acceleration is in good approximation

$$
a_{c_{ref}} = \frac{S\,A}{c\,m}\,(1 + \rho_{\mathrm{Al}})\,, \tag{18}
$$

and the tangential force is

$$
F_{t_{ref}} = 2\left(\frac{S}{c}\right)A\cos^2\alpha\,\sin\alpha\,\rho_{\mathrm{Al}}\,. \tag{19}
$$

Under the described assumptions Table 5 provides the estimated change of the characteristic acceleration and the tangential force due to proton irradiation.

Table 5: Estimated change of characteristic acceleration and tangential force (under $\alpha = 35°$) for the radiated samples.

Sample	Rad. Temp. [°C]	$a_c/a_{c_{ref}}$ [%]	$F_t/F_{t_{ref}}$ ($\alpha = 35°$) [%]
S1	-176	97.18	85.88
S2	-100	96.53	82.67
S3	31.6	99.67	98.39
S4	75	99.00	95.01
S5	113	99.97	99.88

Looking only to the change of the characteristic acceleration might lead to the false impression that the degradation has minor effect, but it needs to be considered that even an purely diffuse reflective sail the characteristic acceleration is not zero and the ratio $a_c/a_{c_{ref}}$ for such a purely diffuse reflective sail is still 89.95%. For a change of orbit energy it is required to generate an orbit tangential force and a loss of specular reflectance has a bigger impact on that tangential force than on the characteristic acceleration.

8. Conclusions

The presented laboratory proton irradiation tests indicate that the reflective properties of aluminized membranes can severely degrade in the interplanetary space environment throughout a solar sail mission.

Direct consequence of the blistering phenomena is a drop of the surface specular reflectivity. The tests indicate that, depending on the temperature, this happens just within a few days of a solar sail mission. In this context it must find strong consideration that the tests presented here correspond to only a few days in space while solar sail missions consider years of operations. The drop of reflectance has a serious consequence for propulsion capabilities of any sailcraft since its acceleration is proportional to reflectivity condition of its membrane material. At the same time total reflectance remains almost constant. One exception in our test was

sample S1 with $\rho_{AL} \sim 0.7$. Within next test campaigns we plan to repeat irradiation tests of samples exposed to protons at cryogenic temperatures in order to confirm this finding.

In that context it seems that the current thermal design of solar sail membranes is in strong contradiction to a design that keeps the temperature higher in order to avoid blistering and loss of specular reflectance. It is for example very often considered to have a chromium coated backside for good infrared emittance and consequently low temperatures. Our tests indicate that such a sail would loose about 17% of its capability to change the orbit within less than three days in a distance of 1 AU from the Sun. However, a good counter measure seems to be to use a membrane that is coated with aluminum on both sides which leads to higher temperature and only a small but measurable loss of specular reflectance.

It must be, however, strongly emphasized that the here described irradiation test took into account just monoenergetic 2.5 keV protons while interplanetary medium is filled up with electrons and ions having a wide range of energy as well as electromagnetic radiation. Its complex and dynamic composition is ruled by the Sun's ~11-years cycle, therefore, true response of the membrane material to the real interplanetary environment is to a great extend unknown.

An interesting perspective idea for future radiation test activity is to verify rather alpha particles (double ionized helium atoms) form blisters filled with molecular helium gas. Sun consists of ~75% hydrogen, ~25% helium, and small portion of other elements. Solar wind has similar proportion of ion composition. Hence, one can expect that helium blisters would grow ~3 times slower than the hydrogen blisters. However, taking fact that typical interplanetary mission last longer than 10 years, as well as taking into account typical timescale for hydrogen blisters growth of just a few days in space, formation of the helium blisters would have significant contribution to overall degradation of any metallic surface exposed to the Sun radiation under interplanetary medium conditions.

One reason that the idea of solar sailing is so attractive for the implementation of innovative missions is that a sailcrafts' life is not limited by the amount of fuel available. Nevertheless, it is uncertain how long the sail membrane can withstand the space environment. At the very least the presented test results show that it cannot be assumed that the reflective properties are not changing. In consequence the next step will be to determine the progression of the blistering formation over time, so that this can find consideration in the mission design process.

Acknowledgements

We would like to thank anonymous reviewers for their careful reading of the manuscript and their many helpful comments and suggestions.

References

Ancona, E., Kezerashvili, R.Y., 2017. Temperature restrictions for materials used in aerospace industry for the near-sun orbits. Acta Astronautica 140, 565–569. doi:10.1016/j.actaastro.2017.09.002.

Dachwald, B., Seboldt, W., Macdonald, M., Mengali, G., Quarta, A., McInnes, C., Rios-Reyes, L., Scheeres, D., Wie, B., Görlich, M., et al., 2005. Potential solar sail degradation effects on trajectory and attitude control, in: AIAA guidance, navigation, and control conference and exhibit, p. 6172. doi:10.2514/6.2005-6172.

Daniels, R.D., 1971. Correlation of hydrogen evolution with surface blistering in poton-irradiated aluminum. Journal of Applied Physics 42, 417–419. doi:10.1063/1.1659613.

Eichler, J., 2005. Lectures on ion-atom collisions, from nonrelativistic to relativistic velocities. Elsevier B.V.

Evertsson, J., Bertram, F., Zhang, F., et al., 2015. The thickness of native oxides on aluminum alloys and single crystals. Applied Surface Science 349, 826–832. doi:10.1016/j.apsusc.2015.05.043.

Fernandez, J., Rose, G., Stohlman, O., Younger, C., Dean, G., Warren, J., Kang, J., Bryant, R., Wilkie, W., 2018. An advanced composites-based solar sail system for interplanetary small satellite missions, AIAA Spacecraft Structures Conference, American Institute of Aeronautics and Astronautics, Kissimmee, FL, USA. doi:10.2514/6.2018-1437.

Hagstrum, H.D., 1965. Theory of auger ejection of electrons from metals by ions. Physical Review 96, 336–365. doi:10.1103/PhysRev.96.336.

Heiligers, J., Diedrich, B., Derbes, W., McInnes, C., 2014. Sunjammer: Preliminary end-to-end mission design, AIAA/AAS Astrodynamics Specialist Conference, San Diego, CA, USA.

Kang, J., Gordon, K., Bryant, R., Stohlman, O., Wilkie, W., Stark, A., Barfield, R., Sindle, B., Finckenor, M., Craven, P., 2019. Durability characterization of mechanical interfaces in solar sail membrane structures, the Fifth International Symposium on Solar Sailing, Aachen, Germany.

Melnik, N., Geppert, U., Biering, B., Lura, F., 2014. Light pressure measurement at dlr bremen, in: Advances in Solar Sailing. Springer, pp. 399–406. doi:10.1007/978-3-642-34907-2_26.

Milacek, L.H., Daniels, R.D., 1968. Proton-radiation-induced blistering of aluminium. Journal of Applied Physics 39, 2803–2815. doi:10.1063/1.1656677.

Myers, S.M., Baskes, M.I., Birnbaum, H.K., et al., 1992. Hydrogen interactions with defacts in crystalline solids. Reviews of Modern Physics 64, 559–617. doi:10.1103/RevModPhys.64.559.

Renger, T., Sznajder, M., Witzke, A., Geppert, U., 2014. The complex irradiation facility at dlr-bremen, in: Macdonald, M. (Ed.), Advances in Solar Sailing. Springer Praxis Books, pp. 541–557. doi:10.1007/978-3-642-34907-2_34.

SILSO World Data Center, 1996-2019. The International Sunspot Number. International Sunspot Number Monthly Bulletin and online catalogue .

Sols, F., Flores, F., 1984. Charge transfer processes for light ions moving in metals. Physical Review B 30, 4478–4880. doi:10.1103/PhysRevB.30.4878.

Sznajder, M., Geppert, U., Dudek, M.R., 2015. Degradation of metallic surfaces under space conditions, with particular emphasis on hydrogen recombination processes. Advances in Space Reserach 56, 71–84. doi:10.1016/j.asr.2015.03.032.

Sznajder, M., Geppert, U., Dudek, M.R., 2018. Hydrogen blistering under extreme radiation conditions. npj Materials Degradation 2, 1–8. doi:10.1038/s41529-017-0024-z.

Wilkie, W., Fernandez, J., Banicevic, P., Stohlman, O., Rose, G., Warren, J., Chamberlain, M., Kang, J., Straubel, M., Heiligers, J., 2019. An overview of nasa's advanced composite solar sail system (acs3) low-earth orbit technology demonstration project, the Fifth International Symposium on Solar Sailing, Aachen, Germany.

Xie, D.G., Wang, Z.J., Sun, J., et al., 2015. In situ study of the initiation of hydrogen bubbles at the aluminium metal/oxide interface. Nature Materials 14, 899–903. doi:10.1038/nmat4336.

Ziegler, J.F., Ziegler, M.D., Biersack, J.P., 2010. SRIM - The stopping and range of ions in matter (2010). Nuclear Instruments and Methods in Physics Research B 268, 1818–1823. doi:10.1016/j.nimb.2010.02.091.